An Occlusion Signal-Processing Framework Based on UAV Sampling for Improving Rendering Quality of Views

Qiuming Liu[1,2(✉)], Ke Yan[1], Yichen Wang[1], RuiQin Li[1], and Yong Luo[3]

[1] School of Software Engineering, Jiangxi University of Science and Technology, Nanchang 330013, China
liugiuming@jxust.edu.cn, 6720210691@mail.jxust.edu.cn
[2] Nanchang Key laboratory of Virtual Digital Factory and Cultural Communications, Nanchang 330013, China
[3] School of Software, Jiangxi Normal University, Nanchang 330022, China

Abstract. Using unmanned aerial vehicles (UAV) for large-scale scene sampling is a prevalent application in UAV vision. However, there are certain factors that can influence the quality of UAV sampling, such as the lack of texture details and drastic changes in scene geometry. One common factor is occlusion, which is a surface feature in 3D scenes that results in significant discontinuity on the scene surface, leading to transient noise and loss of local information. This can cause degradation in the performance of computer vision algorithms. To address these challenges, this paper proposes a UAV sampling method that takes into account occlusion. The method is based on the principle of quantizing occlusion information and improves the aerial light field (ALF) technology. It establishes a UAV ALF sampling model that considers scene occlusion information and calculates the minimum sampling rate of UAV sampling by deriving the exact expression of the spectrum. The proposed model is used to sample and reconstruct large-scale scenes in different occlusion environments. Experimental results demonstrate that the model effectively improves the reconstruction quality of large-scale scenes in occluded environments.

Keywords: Unmanned aerial vehicle · Occlusion scene · Aerial light field · Spectrum analysis

1 Introduction

Using Unmanned Aerial Vehicles (UAV) for image sampling and scene reconstruction is a prevalent application in computer vision [1–5]. UAV sampling offers greater flexibility and a wider sampling range compared to traditional camera sampling in large-scale scenes. However, it also faces some challenges,

C. Wu et al. (Eds.): MONAMI 2023, LNICST 559, pp. 3–15, 2024.
https://doi.org/10.1007/978-3-031-55471-1_1

such as a lack of texture detail, drastic surface changes in the scene, and so on. One particular issue is occlusion - a feature in 3D scenes that causes significant discontinuities on object surfaces, resulting in transient noise and loss of local information. The absence of these crucial details can lead to a degradation in the performance of computer vision algorithms.

To address these challenges and enhance the quality of novel view reconstruction in large-scale scenes, we propose a method based on the quantification of occlusion information. Meanwhile, our proposed method improves the aerial light field (ALF) technique and obtains an ALF sampling model for UAV. This model can reduce the impact of occlusion on large-scale scene reconstruction. The procedures are as follows: First, we conduct an in-depth analysis of the UAV sampling characteristics, based on which we establish the occlusion signal model of the ALF. According to the model, the occlusion degree in the scene is quantified. Then we derive the precise expression of the ALF based on the established sampling model, enabling us to obtain the necessary spectral support for ALF. Additionally, we analyze the signal bandwidth according to spectral support to determine the minimum sampling rate for UAV sampling. Finally, we solve the sampling problem of the real obscured scenes to prove the practicality of the model.

2 Related Work

2.1 UAV Sampling and Rendering

In recent years, there has been a great deal of research about techniques for sampling and reconstructing large-scale scenes from UAV, and these techniques are also widely used in a variety of fields. Schedl *et al.* [6] utilized airborne optical sectioning (AOS) image integration technology to locate missing or injured individuals within dense forests, thereby paving the way for future advancements in search and rescue techniques. Khaloo *et al.* [7] employed UAV-captured images along with SFM algorithms to create three-dimensional (3D) models of bridges for unmanned aerial vehicle inspections. This approach facilitates the evaluation of bridge structural integrity and ensures the safety of transportation infrastructure. Liu *et al.* [8] proposed an image-based crack assessment method for bridge piers using unmanned aerial vehicles and 3D scene reconstruction algorithms. Through this approach, UAV technology is utilized to evaluate and maintain the safety of bridge piers by detecting and analyzing cracks. Prosekov *et al.* [9]developed techniques and software for 3D thermal imaging and mapping of coal warehouses and coal mining facilities. This advancement aims to swiftly identify potential fire ignition points, thus enabling prompt fire prevention measures and minimizing extinguishing time. Fernando *et al.* [10] implemented a UAV photogrammetry scheme based on Structure from Motion (SfM) and Multiple View Stereo (MVS) algorithms. By utilizing this method, they successfully modeled the topography of surfaces, established structural foundations, and connecting channels. The resulting data aided in reconstructing and understanding

intricate archaeological sites, ultimately contributing to their restoration and preservation.

To improve the quality of UAV image reconstruction, various methods have been proposed to make an improvement, especially for the prevalent occlusion problem in large-scale scenes, Guan *et al.* [11] introduced a UAV-YOLO vehicle detector that utilizes depth-separable convolution and resolution adjustment techniques. They also proposed a multi-view occlusion optimization algorithm to enhance the quality and speed of reconstruction by determining the optimal spatial distribution of image sequences. Schneider *et al.* [12] developed a TLS-based 3D structure measurement method specifically designed for dense tropical and temperate forests. This approach effectively quantifies the 3D structure and occlusion within the forests, resulting in improved quality for 3D measurement and reconstruction of forest environments. Zhao *et al.* [13] put forth an improved YOLOV5 method for accurate detection of wheat spikes in UAV images. This method addresses the issue of occlusion-induced spike detection errors and missed detections, leading to more reliable and precise results.

These works have made significant contributions to the research on sampling and reconstruction of UAVs for large scenes. However, it is worth noting that there has been limited focus on specific factors that are prevalent in large-scale scenes, such as occlusion and shadows. These factors play a crucial role in the overall quality of sampling and reconstruction in large-scale scenes. Furthermore, some reconstruction methods that overlook the sampling rate while prioritizing the enhancement of reconstruction quality. This oversight often results in data redundancy and consumes excessive memory during the reconstruction process.

2.2 Light Field Sampling and Reconstruction

With the increasing application of 3D reconstruction and other technologies, many related methods have been proposed to reduce the sampling rate of light field and improve the rendering quality of view. To reduce the redundancy of light field sampling and improve the reconstruction efficiency, Qi *et al.* [14] proposed the feature ray under-sampling (FRUS) method, and studied the influence of the under-sampling methods, flame dividing voxels, noise levels and light field camera parameters. Gilliam *et al.* [15] employed a set of inclined planes to approximate the scene's geometry and derived a precise closed expression for the complete optical spectrum of a finite width inclined plane. Additionally, they developed a novel reconstruction filter to enhance the reconstruction process. Wu *et al.* [16] conducted a study and discovered that the fundamental issue behind the challenges of large disparities and non-Lambertian surfaces is the problem of aliasing. They introduced an alternative framework for performing anti-aliasing reconstruction in the image domain, which demonstrated excellent results.

Although there have been many researches related to light field sampling and reconstruction, the techniques related to light field reconstruction are still limited to small scenes.

3 A Framework for Occlusion Signal Based on UAV Sampling

3.1 Aerial Light Field Parameterization

For light rays, a 7-dimensional function(POF) $\Phi(x, y, z, \theta, \phi, \lambda, \tau)$ [17] is usually used to parameterize it (Fig. 1), where(x, y, z) is the position of the UAV, (θ, ϕ) is the direction of light transmission, λ is the wavelength of the rays and τ is the time.

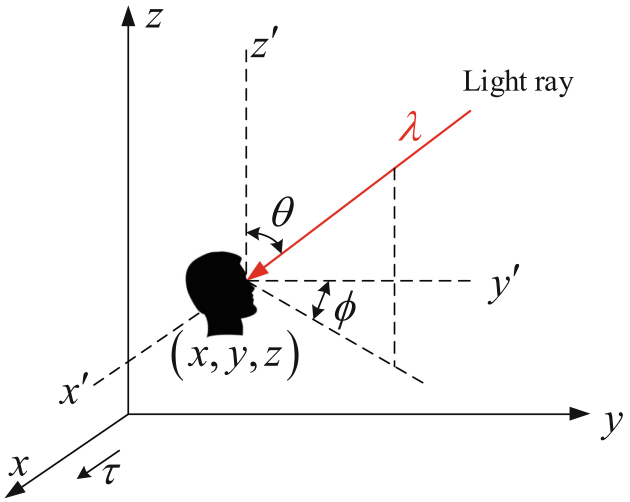

Fig. 1. 7-dimensional plenoptic function. A light in space is described with seven parameters centered on the human eye.

The 7D functions are complex when it comes to mathematical calculations and Fourier transforms. Therefore, it can be simplified to 5D in the process of describing the actual 3D scene, as $F(x, y, z, \theta, \phi)$.

3.2 Aerial Light Field Occlusion Signal Model

In this paper, we analyse the scene information captured by the UAV to quantify the degree of occlusion in the scene. The field of view (FOV) of the UAV camera represents the range of scene information that can be captured, as shown in Fig. 2. The FOV can be represented by cone $U-ABCD$, $U(x, y, z, \theta, \phi)$represents the information captured by the camera, and the occlusion field is represented by cone $U - A'B'C'D'$. Obviously the occlusion field is also a part of the FOV.

Zhu *et al.* in the literature [18], define a novel view of the rendering of the captured scene information based on the camera to improve the rendering quality

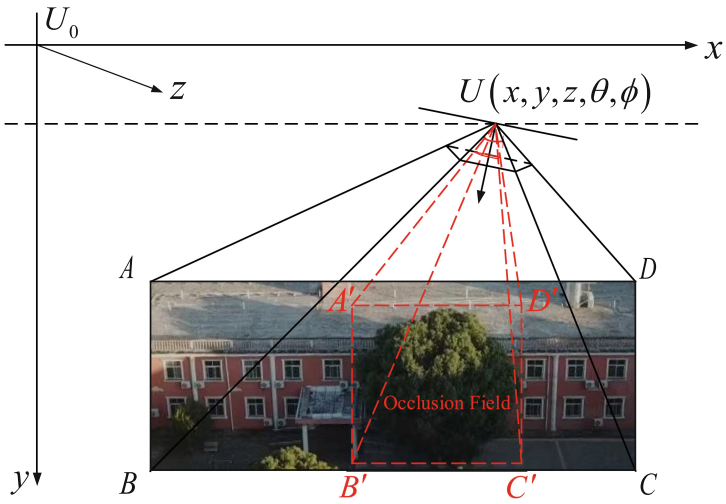

Fig. 2. 3D Aerial light field occlusion signal model. The red box area indicates the occlusion coverage range in the scene. (Color figure online)

by compensating for the OCD function [19]. The expressions are as follows,

$$P(x,y,z,\theta,\phi) = \int \Phi\left(C(x,y,z,\theta,\phi), O(x,y,z,\theta,\phi)\right) \cdot B(x,y,z,\theta,\phi)\, dxdydzd\theta d\phi \tag{1}$$

where $P(x,y,z,\theta,\phi)$ represents the new view after rendering, $C(x,y,z,\theta,\phi)$is the scene information captured by the UAV, $\Phi(\cdot)$ is a compensation function implemented in a certain relationship, and $B(\cdot)$ is the rendering kernel function. The function $O(x,y,z,\theta,\phi)$ represents the degree of occlusion in the scene captured by the UAV. The expression for $O(x,y,z,\theta,\phi)$ is as follows,

$$O(x,y,z,\theta,\phi) = \beta \frac{V_O(x,y,z,\theta,\phi)}{V_F(x,y,z,\theta,\phi)} \tag{2}$$

where β is determined by the FOV $V_F(x,y,z,\theta,\phi)$ of the UAV. $V_F(x,y,z,\theta,\phi)$and $V_O(x,y,z,\theta,\phi)$are the volumes of cone $U-ABCD$ and cone $U-A'B'C'D'$. Based on this theory, we develop an ALF occlusion signal model. In order to improve the computational efficiency and reduce the complexity of the quantitative expression of occlusion, we further simplify the 5D light field according to the principle of unstructured light fields [20]. By choosing a position parameter $(x,z)$and a direction parameter θ, the 5D function is then reduced to a 3D function. The expression (1) is simplified as follows,

$$P(x,z,\theta) = \int \Phi\left(C(x,z,\theta), O(x,z,\theta)\right) \cdot B(x,z,\theta)\, dxdzd\theta \tag{3}$$

Thus, the model in Fig. 2 can be simplified to Fig. 3, where the degree of occlusion can be expressed as the ratio of the area of the occlusion field to the area of the FOV, and their area can be quantified in terms of the number of rays.

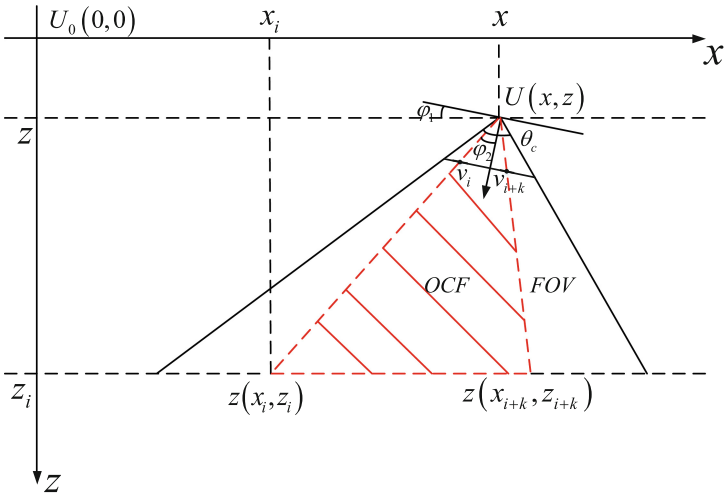

Fig. 3. 2D Aerial light field occlusion signal model. The red box region represents the set of rays of the occluded range. (Color figure online)

The light rays can be defined by their intersection with the camera plane at position x and imaging planes corresponding to pixel position v [15]. Thus there is,

$$\tan\varphi_2 = \tan\left(90^\circ - (\varphi_1 + \theta_1)\right) = \frac{\cos\varphi_1\left(x_0 - x_1\right) - \sin\varphi_1\left(z_1 - z_0\right)}{\sin\varphi_1\left(x_0 - x_1\right) + \cos\varphi_1\left(z_1 - z_0\right)} \tag{4}$$

$$v = f\tan\varphi_2 = f\left(\frac{\cos\varphi_1\left(x_0 - x_1\right) - \sin\varphi_1\left(z_1 - z_0\right)}{\sin\varphi_1\left(x_0 - x_1\right) + \cos\varphi_1\left(z_1 - z_0\right)}\right) \tag{5}$$

From this we get an exact expression for the pixel position, which we can then substitute into a simplified expression for the degree of occlusion. Finally, we get the expression of scene occlusion degree expressed by UAV position and pitch angle.

$$\begin{aligned} O\left(x,z,v\right) &= \beta\frac{K\left(x,z,v\right)}{N\left(x,z,v\right)} \approx \beta\frac{\left|v_{i+k} - v_i\right|}{2v_m} \\ &= \frac{\beta}{2f\tan\frac{\theta_c}{2}}\left|\frac{f\cos\varphi_1\left(x - x_i\right) + f\sin\varphi_1\left(z - z_i\right)}{\sin\varphi_1\left(x - x_i\right) + \cos\varphi_1\left(z_i - z\right)} - \frac{f\cos\varphi_1\left(x - x_{i+k}\right) + f\sin\varphi_1\left(z - z_{i+k}\right)}{\sin\varphi_1\left(x - x_{i+k}\right) + \cos\varphi_1\left(z_{i+k} - z\right)}\right| \end{aligned} \tag{6}$$

where f is the distance between the camera plane and the image plane, as the focal length. φ_2 is the pitch angle of the unmanned aerial vehicles. v_m is the maximum pixels in the image plane.

3.3 Fourier Transform of the ALF Occlusion Signal Model

A spectral transformation of the sampling model of the occlusion signal allows the effect of occlusion on the signal to be analyzed, and a Fourier transform of the occlusion function gives as follows,

$$O(\omega_x,\omega_z,\omega_v)=\int_{-\infty}^{\infty}\int_{-\infty}^{\infty}\int_{-\infty}^{\infty}O(x,z,v)\times\exp\left(-j\left(\omega_x x+\omega_z z+\omega_v v\right)\right)dxdzdv \tag{7}$$

where the $E=\exp\left(-j\left(\omega_x x+\omega_z z+\omega_v v\right)\right)$, and in the following we will abbreviate $O(\omega_x,\omega_z,\omega_v)$ to $O(\cdot)$. Substituting (6) into (7) and we get,

$$\begin{aligned}O(\cdot)&=\iiint\frac{\beta E}{2f\tan\frac{\theta_c}{2}}\left[\begin{array}{l}\dfrac{f\cos\varphi_1(x-x_i)+f\sin\varphi_1(z-z_i)}{\sin\varphi_1(x-x_i)+\cos\varphi_1(z_i-z)}-\\ \dfrac{f\cos\varphi_1(x-x_{i+k})+f\sin\varphi_1(z-z_{i+k})}{\sin\varphi_1(x-x_{i+k})+\cos\varphi_1(z_{i+k}-z)}\end{array}\right]dxdzdv\\&=\frac{\beta}{2f\tan\frac{\theta_c}{2}}\left[\begin{array}{l}\iiint\dfrac{f\cos\varphi_1(x-x_i)+f\sin\varphi_1(z-z_i)}{\sin\varphi_1(x-x_i)+\cos\varphi_1(z_i-z)}Edxdzdv\\ -\iiint\dfrac{f\cos\varphi_1(x-x_{i+k})+f\sin\varphi_1(z-z_{i+k})}{\sin\varphi_1(x-x_{i+k})+\cos\varphi_1(z_{i+k}-z)}Edxdzdv\end{array}\right]\end{aligned} \tag{8}$$

By analyzing (8) and applying properties of calculus, we decompose it into two triple integrals. We further proceed to decompose and simplify each triple integral, taking into account the symmetry of the Fourier transform. Ultimately, we obtain formula (9), which represents the spectral expression of the occlusion function.

$$\begin{aligned}O(\cdot)=&\frac{j\beta\pi^2\operatorname{sgn}(\omega_x)}{f\cdot\tan\theta_c/2}\left(\begin{array}{l}\exp\left(j\omega_x\left(\dfrac{\omega_v-\omega_x d_{i+K}-\omega_z t_{i+K}}{\omega_z}\right)\right)(x_{i+K}+d_{i+K})\\ -\exp\left(j\omega_x\left(\dfrac{\omega_v-\omega_x d_i-\omega_z x_i}{\omega_z}\right)\right)(x_i+d_i)\end{array}\right)\\&+\pi^2 f\begin{pmatrix}1+\pi\delta(\omega_v-2)\\ +\pi\delta(\omega_v+2)\end{pmatrix}\left(\begin{array}{l}\left(\begin{array}{l}\dfrac{d_i\delta(\omega_z)\operatorname{sgn}(\omega_x)-j\delta'(\omega_z)\operatorname{sgn}(\omega_x)}{\omega_x}+\\ \dfrac{d_i\delta(\omega_x)\operatorname{sgn}(\omega_z)-j\delta'(\omega_x)\operatorname{sgn}(\omega_z)}{\omega_z}\end{array}\right)\\ -\left(\begin{array}{l}\dfrac{d_{i+K}\delta(\omega_z)\operatorname{sgn}(\omega_x)-j\delta'(\omega_z)\operatorname{sgn}(\omega_t)}{\omega_x}+\\ \dfrac{d_{i+K}\delta(\omega_x)\operatorname{sgn}(\omega_z)-j\delta'(\omega_x)\operatorname{sgn}(\omega_z)}{\omega_z}\end{array}\right)\end{array}\right)\\&+j\pi^2\left(\delta(\omega_v+2)-\delta(\omega_v-2)\right)\left(\begin{array}{l}\left(\begin{array}{l}\delta(\omega_z)\left(t_i\operatorname{sgn}(\omega_x)-2\pi\delta(\omega_x)\right)\\ +\left(t_i\operatorname{sgn}(\omega_z)-2\pi\delta(\omega_z)\right)\end{array}\right)\\ -\left(\begin{array}{l}\delta(\omega_z)\left(t_{i+K}\operatorname{sgn}(\omega_x)-2\pi\delta(\omega_x)\right)\\ +\left(t_{i+K}\operatorname{sgn}(\omega_z)-2\pi\delta(\omega_z)\right)\end{array}\right)\end{array}\right)\end{aligned} \tag{9}$$

3.4 ALF Occlusion Signal Sampling and Reconstruction

The spectrum of the occlusion function from (9) contains ω_x, ω_z and ω_v. Where ω_z depends on the depth between the UAV and the subject. We only analyze the occlusion function through ω_x and ω_v. Applying the concept of fundamental bandwidth, the bandwidths along the ω_x-axis and the ω_v-axis of the occlusion function are derived as follows,

$$B_x = \left\{ \omega_x : |\omega_x| \leq \frac{1}{2\pi \left| x_i - x_{i+k} \right| \cdot \left| d_i - d_{i+k} \right| + \operatorname{sgn}(\theta)} \right\} \tag{10}$$

$$B_v = \left\{ \omega_v \in \left[\frac{\Omega_x \left| x_i - x_{i+k} \right| z_{\max}}{f}, \frac{\Omega_x \left| x_i - x_{i+k} \right| z_{\min}}{f} \right] \right\} \tag{11}$$

where Ω_x denotes the maximum value of B_x along the ω_x-axis, as

$$\Omega_x = \frac{1}{2\pi \left| x_i - x_{i+k} \right| \cdot \left| d_i - d_{i+k} \right| + \operatorname{sgn}(\theta)} \tag{12}$$

Depending on the bandwidth, an adaptive filter is designed to eliminate the interference caused by the occlusion signal. Tilting filter is still used in the reconstruction, with two filter expressions are as follows,

$$H_{opt}(\omega_x, \omega_v) = \frac{F^*((\omega_x + \omega_v))}{B_x + B_v} e^{-j(\omega_x T_x + \omega_v T_v)} \tag{13}$$

$$F_R = \frac{\left| x_i - x_{i+k} \right| \cdot \left| z_{\max} + z_{\min} \right|}{2\pi f} \tag{14}$$

Referring to the occlusion scoring method proposed by Zhu *et al.* in the literature [18], the case where occlusion has the least impact on the quality of the scene reconstruction can be deduced. The expression for the occlusion scoring is as follows,

$$S_R = \min_{(x,z,v)} \left(\hat{O}(x, z, v) \right) = \min_{(x,z,v)} \left(\frac{\left| v_{i+k} - v_i \right|}{2f \cdot \tan \theta_c / 2} \right) = \min_{x=x_0, \theta=\theta_0} \left(\frac{\left| v_{i+k} - v_i \right|}{2f \cdot \tan \theta_c / 2} \right) \tag{15}$$

4 Experiment

4.1 Experimental Sampling Methods

The experiment of large-scale aerial shooting scene conducted in this paper is based on the mathematical theory derivation above. By determining the spectral bandwidth of ALF, the maximum sampling spacing of UAV sampling can be deduced, that is, the minimum sampling rate can be obtained, and the reconstruction filter can be obtained at the same time. According to the minimum sampling rate, the sampling interval can be determined. The inter-frame estimation method in [21] takes frames from the UAV sampling video to obtain the images required for the experiment, and then renders new views according to the sampled images.

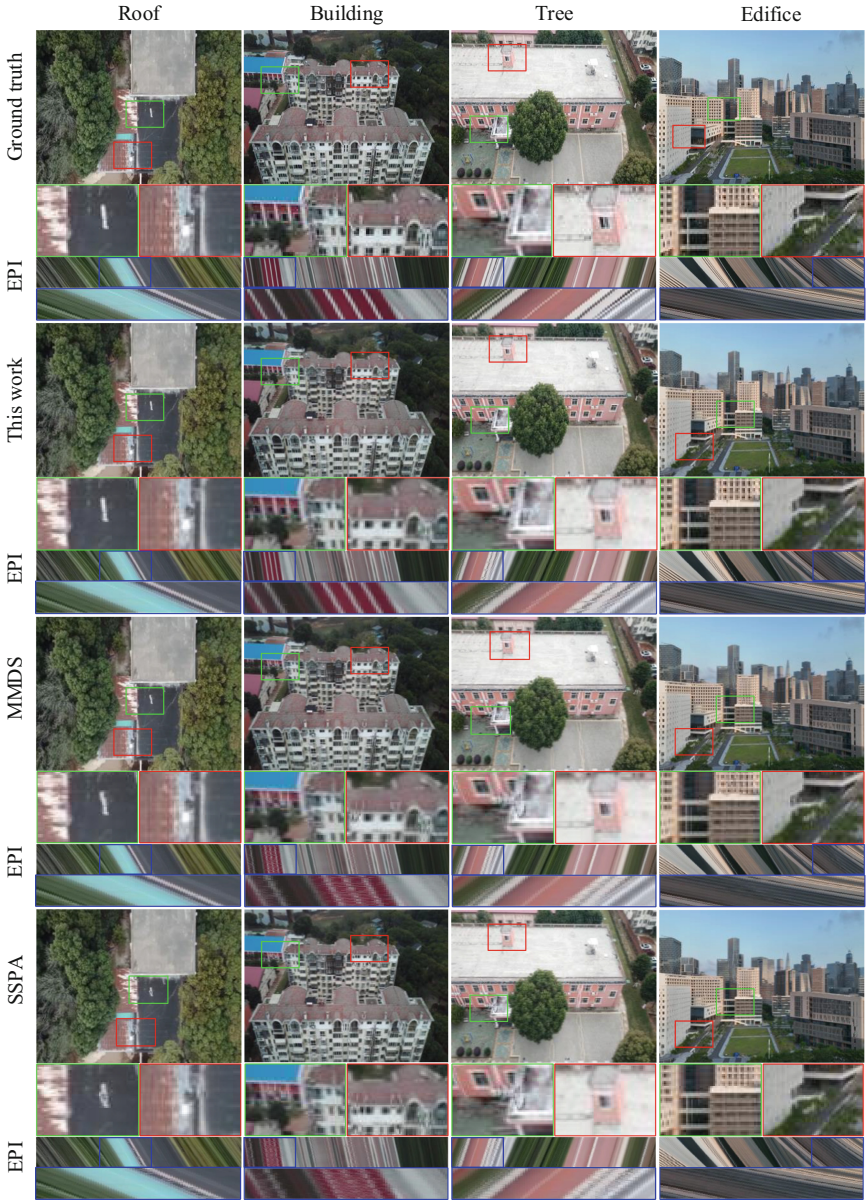

Fig. 4. Experiment with novel view reconstruction of complex real scenes. Different sampling methods have different quality results for four different experimental scenarios. Changes in EPI can reflect the quality of the reconstructed view by the corresponding method. Some Magnified details help us to clearly compare the rendering quality of different methods.

4.2 Real Scene Experiment

In this experiment, we selected several different types of occlusion scenes and successfully reconstructed them. These scenes involved various scenarios, such as trees obstructing buildings, multiple buildings obstructing each other, and unique vertical views in aerial scenes. To ensure the credibility of our findings, we conducted comparative experiments with other relevant methods, including Maximum and Minimum Depth of the Scene (MMDS) [22] and Single Slanted Plane Analysis (SSPA) [15]. Additionally, we employed the EPI (Epipolar Plane Image) [23] to verify the view reconstruction quality of different methods.

As depicted in Fig. 4, we present the reconstructed views and corresponding EPIs of four scenes for comparison. Notably, these scenes featured large-scale dimensions and intricate surface textures, representing a key characteristic of complex aerial photography scenes. The results demonstrate that the proposed sampling method in this study significantly enhances the quality of reconstructed views, particularly when considering the occlusion present in real-world scenes. This indicates the effectiveness of our proposed sampling method for large-scale complex aerial photography scenes. Moreover, when zooming in on specific scene details, it becomes evident that our proposed method also outperforms other approaches in terms of reconstruction accuracy.

Table 1. PSNRs for rendering of four real scenes using three different methods.

Method	Scene			
	Roof	Building	Tree	Edifice
This work	30.413	27.696	28.306	27.083
MMDS	29.564	26.735	27.415	26.374
SSPA	29.222	26.466	27.105	26.095

Table 2. SSIMs for rendering of four real scenes using three different methods.

Method	Scene			
	Roof	Building	Tree	Edifice
This work	0.889	0.914	0.890	0.897
MMDS	0.861	0.890	0.858	0.872
SSPA	0.850	0.883	0.847	0.867

To intuitively compare the rendering quality of different methods, we compared the Peak Signal-to-Noise Ratio (PSNR) and Structural Similarity Index (SSIM) of four sets of experiments, and the average values of the PSNR and SSIM are shown in Table 1 and Table 2. By comparing the Peak Signal-to-Noise Ratio (PSNR) and Structural Similarity Index (SSIM) obtained from our real scene

experiments, we observe that the UAV sampling method proposed in this paper consistently produces superior rendering effects for generating novel viewpoints. This result further proves the superiority of our sampling method. Overall, the experimental results affirm the reconstruction capabilities of the UAV sampling method across a wide range of scene types.

5 Conclusion

Based on the principle of quantizing occlusion information, this paper presents a novel UAV sampling method that considers occlusion to improve the technology of ALF. We establish a UAV ALF sampling model that takes into account scene occlusion information, enabling us to calculate the minimum sampling rate required for UAV sampling by deriving the exact expression of the spectrum. Additionally, we determine the reconstruction filter suitable for large-scale aerial photography. The experimental results demonstrate the model's effectiveness in mitigating the impact of occlusion on large-scale scene reconstruction, and shows the superiority of this model in reconstructing large-scale scenes in occluded environment.

However, it is important to note that our discussion solely focuses on the UAV sampling method considering occlusion. During the ALF sampling process, the presence of sunlight can create shadow areas within the scene, while light reflections may occur on the external walls of certain buildings. These factors can potentially impact the overall quality of scene reconstruction for large-scale scenes. In our future research, we will focus on exploring various improvement methods to further enhance the quality of occlusion scene novel view reconstruction.

Acknowledgment. This work was supported in part by National Natural Science Foundation of China (No. 62067003), in part by Culture and Art Science Planning Project of Jiangxi Province (No. YG2018042), in part by Humanities and Social Science Project of Jiangxi Province (No. JC18224).

References

1. Yan, F., Xia, E., Li, Z., Zhou, Z.: Sampling-based path planning for high-quality aerial 3D reconstruction of urban scenes. Remote Sens. **13**(5) (2021). https://doi.org/10.3390/rs13050989. https://www.mdpi.com/2072-4292/13/5/989
2. He, Y., Liang, Q., Lu, H., Chai, C.: Based on unmanned aerial vehicle real-scene 3D design and implementation of virtual simulation experiment system for mine smart supervision in large-scale applications. In: 2021 2nd International Conference on Information Science and Education (ICISE-IE), pp. 1406–1413. IEEE (2021)
3. Hermawan, S., Purnomo, J., Tjandra, D., Purnomo, Y.C.: The use of unmanned aerial vehicles (UAV) for reconstruction of topography and bathymetry maps: consideration for civil construction against coastal adaptation due to climate changing. In: MISEIC 2018 (2018)

4. Mancini, F., Dubbini, M., Gattelli, M., Stecchi, F., Fabbri, S., Gabbianelli, G.: Using unmanned aerial vehicles (UAV) for high-resolution reconstruction of topography: the structure from motion approach on coastal environments. Remote Sens. **5**(12), 6880–6898 (2013)
5. Qiao, G., Yuan, X., Florinsky, I., Popov, S., He, Y., Li, H.: Topography reconstruction and evolution analysis of outlet glacier using data from unmanned aerial vehicles in Antarctica. Int. J. Appl. Earth Obs. Geoinf. **117**, 103186 (2023)
6. Schedl, D.C., Kurmi, I., Bimber, O.: Search and rescue with airborne optical sectioning. Nat. Mach. Intell. **2**(12), 783–790 (2020)
7. Khaloo, A., Lattanzi, D., Cunningham, K., Dell'Andrea, R., Riley, M.: Unmanned aerial vehicle inspection of the placer river trail bridge through image-based 3D modelling. Struct. Infrastruct. Eng. 1–13 (2018)
8. Liu, Y.F., Nie, X., Fan, J.S., Liu, X.G.: Image-based crack assessment of bridge piers using unmanned aerial vehicles and three-dimensional scene reconstruction. Comput.-Aided Civ. Infrastruct. Eng. **35**(5), 511–529 (2020)
9. Prosekov, A.Y., Rada, A., Kuznetsov, A., Timofeev, A., Osintseva, M.: Environmental monitoring of endogenous fires based on thermal imaging and 3D mapping from an unmanned aerial vehicle. In: IOP Conference Series: Earth and Environmental Science, vol. 981, p. 042016. IOP Publishing (2022)
10. Carvajal-Ramírez, F., Navarro-Ortega, A.D., Agüera-Vega, F., Martínez-Carricondo, P., Mancini, F.: Virtual reconstruction of damaged archaeological sites based on unmanned aerial vehicle photogrammetry and 3D modelling. Study case of a Southeastern Iberia production area in the bronze age. Measurement **136**, 225–236 (2019)
11. Guan, J., et al.: Full field-of-view pavement stereo reconstruction under dynamic traffic conditions: incorporating height-adaptive vehicle detection and multi-view occlusion optimization. Autom. Constr. **144**, 104615 (2022)
12. Schneider, F.D., Kükenbrink, D., Schaepman, M.E., Schimel, D.S., Morsdorf, F.: Quantifying 3D structure and occlusion in dense tropical and temperate forests using close-range lidar. Agric. Forest Meteorol. **268**, 249–257 (2019). https://doi.org/10.1016/j.agrformet.2019.01.033. https://www.sciencedirect.com/science/article/pii/S0168192319300267
13. Zhao, J., et al.: A wheat spike detection method in UAV images based on improved YOLOv5. Remote Sens. **13**(16) (2021). https://doi.org/10.3390/rs13163095. https://www.mdpi.com/2072-4292/13/16/3095
14. Qi, Q., Hossain, M.M., Li, J.J., Zhang, B., Li, J., Xu, C.L.: Approach to reduce light field sampling redundancy for flame temperature reconstruction. Opt. Express **29**(9), 13094–13114 (2021)
15. Gilliam, C., Dragotti, P.L., Brookes, M.: On the spectrum of the plenoptic function. IEEE Trans. Image Process. **23**(2), 502–516 (2013)
16. Wu, G., Liu, Y., Fang, L., Chai, T.: Revisiting light field rendering with deep anti-aliasing neural network. IEEE Trans. Pattern Anal. Mach. Intell. **44**(9), 5430–5444 (2021)
17. Adelson, E.H., Bergen, J.R., et al.: The plenoptic function and the elements of early vision. Comput. Models Vis. Process. **1**(2), 3–20 (1991)
18. Zhu, C., Zhang, H., Liu, Q., Zhuang, Z., Yu, L.: A signal-processing framework for occlusion of 3D scene to improve the rendering quality of views. IEEE Trans. Image Process. **29**, 8944–8959 (2020)
19. Durand, F., Holzschuch, N., Soler, C., Chan, E., Sillion, F.X.: A frequency analysis of light transport. ACM Trans. Graph. (TOG) **24**(3), 1115–1126 (2005)

20. Buehler, C., Bosse, M., McMillan, L., Gortler, S., Cohen, M.: Unstructured Lumigraph rendering. In: Proceedings of the 28th Annual Conference on Computer Graphics and Interactive Techniques, pp. 425–432 (2001)
21. Liu, Q., Wang, Y., Wei, Y., Xie, L., Zhu, C., Zhou, R.: Spectral analysis of aerial light field for optimization sampling and rendering of unmanned aerial vehicle. In: 2022 IEEE International Conference on Visual Communications and Image Processing (VCIP), pp. 1–5. IEEE (2022)
22. Chai, J.X., Tong, X., Chan, S.C., Shum, H.Y.: Plenoptic sampling. In: Proceedings of the 27th Annual Conference on Computer Graphics and Interactive Techniques, SIGGRAPH 2000, pp. 307–318. ACM Press/Addison-Wesley Publishing Co., USA (2000). https://doi.org/10.1145/344779.344932
23. Bolles, R.C., Baker, H.H., Marimont, D.H.: Epipolarplane image analysis: an approach to determining structure from motion. Int. J. Comput. Vis. **1**(1), 7–55 (1987)